14th International Symposium on Turbulence and Shear Flow Phenomena (TSFP14)
Heidelberg, Germany, July 28–31, 2026

NUMERICAL SIMULATIONS OF INERTIAL PARTICLE CLUSTERING IN NON-EQUILIBRIUM TURBULENT FLOWS

Taketo Tominaga
Department of Mechanical Engineering
Engineering School, Institute of Science Tokyo
Tokyo, Japan
tominaga.t.2d38@m.isct.ac.jp

Ryo Onishi
Supercomputing Research Center
Institute of Integrated Research, Institute of Science Tokyo
Tokyo, Japan
onishi.ryo@scrc.iir.isct.ac.jp

ABSTRACT
Inertial particles in turbulent flows appear in a wide range of geophysical and industrial applications, including cloud droplets in atmospheric turbulence. Several parameterization models have been proposed to incorporate clustering effects into cloud microphysics schemes, all of which rely on instantaneous equilibrium assumptions that are inapplicable to non-equilibrium atmospheric turbulence. In this study, we investigate inertial particle clustering in non-equilibrium turbulence using direct numerical simulation. We generate non-equilibrium turbulent flows using unsteady step forcing and quantify the relaxation time and hysteresis of the radial distribution function at contact $g(r=R)$. The turbulent flow generated by unsteady step forcing exhibited non-equilibrium scaling. The relaxation time of $g(r=R)$ in response to changes in turbulent energy, τ_g, was estimated to be 3–4 T_e. When the forcing period was longer than or comparable to τ_g, $g(r=R)$ exhibited history dependence and hysteresis. In some cases, $g(r=R)$ ranged from 0.6 to 1.2 times the value predicted by the instantaneous equilibrium model for the same energy dissipation rate. These results indicate that equilibrium-based models cannot accurately predict clustering in non-equilibrium turbulence when the forcing period is comparable to or larger than τ_g, and suggest that constructing a clustering model that accounts for τ_g is essential.

Introduction
Inertial particles in turbulent flows appear in a wide range of geophysical and industrial applications, including cloud droplets in atmospheric turbulence, dust particles in protoplanetary disks, and fuel droplets in spray combustion. Due to the centrifugal effect of turbulent vortices, particles are swept out from high-vorticity regions and concentrate in low-vorticity regions, forming nonuniform spatial distributions known as clustering (Maxey, 1987; Squires & Eaton, 1991). In atmospheric flows, clustering of cloud droplets increases collision and coalescence frequency in raindrop formation (Ireland *et al.*, 2016).

Several parameterization models have been proposed to incorporate clustering effects into cloud microphysics schemes (Ayala *et al.*, 2008; Rosa *et al.*, 2013; Onishi & Seifert, 2016). These models assume that clustering responds instantaneously to changes in turbulent energy and reaches equilibrium states. However, real atmospheric turbulence is often non-equilibrium due to rapid changes in turbulent energy induced by phenomena such as mountain waves and convective updrafts. In reality, clustering responds to these changes with a finite relaxation time. These instantaneous equilibrium models would be therefore inapplicable to non-equilibrium atmospheric turbulence. Understanding clustering in non-equilibrium turbulence is essential for improving model accuracy.

In this study, we investigate inertial particle clustering in non-equilibrium turbulence using direct numerical simulation. We generate non-equilibrium turbulent flows using unsteady step forcing. We quantify the relaxation time and hysteresis of the radial distribution function at contact $g(r=R)$, a standard measure of clustering intensity, under step changes in turbulent energy.

Direct Numerical Simulation
The governing equations for the carrier fluid are the continuity equation and the incompressible Navier–Stokes equations:

$$\nabla \cdot \mathbf{U} = 0, \tag{1}$$

$$\frac{\partial \mathbf{U}}{\partial t} + (\mathbf{U}\cdot\nabla)\mathbf{U} = -\frac{1}{\rho}\nabla p + \nu\nabla^2\mathbf{U} + \mathbf{F}(\mathbf{x},t), \tag{2}$$

where $\mathbf{U}$ is the fluid velocity, ρ is the density, p is the pressure, ν is the kinematic viscosity, and $\mathbf{F}$ is the external forcing. The kinematic viscosity was set to $\nu = 1.5\times10^{-5}$ m^2 s^{-1}, corresponding to atmospheric conditions (1013 hPa, 298 K). The governing equations were discretized on a uniform Cartesian grid with variables stored in a marker-and-cell (MAC) arrangement (Harlow & Welch, 1965). The conservative fourth-order central difference scheme (Morinishi *et al.*, 1998) was applied to the convection term. Time integration was performed using a second-order Runge–Kutta method. Pressure–velocity coupling was handled by the Highly Simplified Marker and Cell (HSMAC) scheme (Hirt & Cook, 1972). The computational domain was a cube of side $2\pi L_0$ with periodic boundary conditions in all directions. All lengths, velocities, and times were non-dimensionalized using L_0, U_0, and L_0/U_0, respectively. The bulk Reynolds number was defined as $Re = U_0 L_0/\nu$.

Particle motion is governed by the following equations:

$$\frac{d\mathbf{X}}{dt} = \mathbf{V}, \tag{3}$$

$$\frac{d\mathbf{V}}{dt} = -\frac{f}{\tau_p}\left(\mathbf{V} - \mathbf{U}(\mathbf{X},t)\right), \tag{4}$$

where $\mathbf{X}$ and $\mathbf{V}$ are the particle position and velocity, and $\mathbf{U}(\mathbf{X},t)$ is the fluid velocity at the particle position. The particle relaxation time is $\tau_p = \frac{2}{9}(\rho_p/\rho)(r^2/\nu)$, where r is the particle radius and ρ_p is the particle density. The particle-to-fluid density ratio was set to $\rho_p/\rho = 843$, corresponding to water droplets under atmospheric conditions (1013 hPa, 298 K). The nonlinear drag correction factor f follows Rowe & Henwood (1961):

$$f = 1 + 0.15 Re_p^{0.687}, \tag{5a}$$

$$Re_p = \frac{2r|\mathbf{V} - \mathbf{U}(\mathbf{X})|}{\nu}. \tag{5b}$$

The fluid velocity at the particle position was computed by trilinear interpolation. Time integration was performed using a second-order Runge–Kutta method. The simulations were performed using LCS.jl (Lagrangian Cloud Simulator in Julia) (Tominaga & Onishi, 2025).

Unsteady Step Forcing

Turbulence was sustained by a forcing scheme based on Reduced Communication Forcing (RCF) (Onishi *et al.*, 2011). The amplitude of $\mathbf{F}$ was controlled so that the energy injection rate P remained constant at a prescribed value. To generate non-equilibrium turbulence, P was modulated as a step function alternating between a strong state $P_{\text{strong}} = 0.8$ and a weak state $P_{\text{weak}} = 0.2$. Two forcing protocols were employed. In fixed-interval forcing, the switching interval was fixed at T, with equal time spent in each state. In random-interval forcing, the residence time in each state was drawn independently from an exponential distribution with mean λ.

Results and Discussion

Figure 1 shows C_ε as a function of Re_λ under fixed-interval forcing for three normalized forcing periods $T^* \equiv T/T_e$, where $T_e \equiv L/u'$ is the eddy turnover time, L is the integral length scale, and u' is the root-mean-square velocity fluctuation. Here, $C_\varepsilon \equiv \varepsilon L/u'^3$, where ε is the energy dissipation rate. $Re_\lambda \equiv u'\lambda/\nu$, where λ is the Taylor microscale and ν is the kinematic viscosity. For long-period forcing ($T^* = 24.0$), four distinct states are identified.States 1 and 3 correspond to the weak and strong turbulence phases, respectively, where $C_\varepsilon \approx 0.5$, consistent with equilibrium dissipation scaling. States 2 and 4 correspond to the weak-to-strong and strong-to-weak transitions, respectively, where $C_\varepsilon \propto Re_\lambda^{-1}$, consistent with non-equilibrium dissipation scaling (Goto & Vassilicos, 2015). For intermediate-period forcing ($T^* = 6.4$), the trajectory follows $C_\varepsilon \propto Re_\lambda^{-1}$ throughout the cycle, indicating that non-equilibrium dissipation persists continuously.

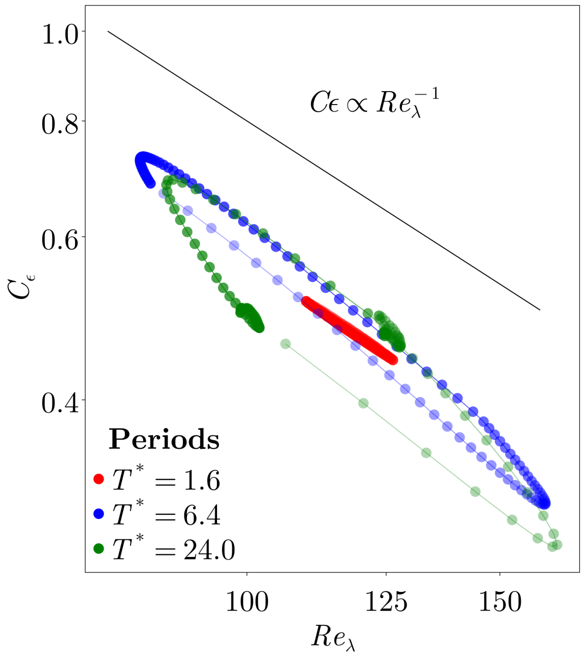

Figure 1. C_ε as a function of Re_λ under fixed-interval forcing for three normalized forcing periods T^*. Color shading indicates temporal evolution, with darker colors representing later times.

For short-period forcing ($T^* = 1.6$), the variations in both Re_λ and C_ε are small, and no non-equilibrium scaling is observed. This demonstrates that unsteady step forcing can generate non-equilibrium turbulence.

Table 1 shows the relaxation time of the radial distribution function at contact, $g(r = R)$, in response to changes in turbulent energy under random-interval forcing with mean switching interval $\lambda = 2.0$. The eddy turnover time was $T_e = 1.0$. The lag between two signals $x(t)$ and $y(t)$ was defined as the time shift that maximizes the cross-correlation function:

$$\tau = \arg\max_{\Delta t} C(\Delta t) = \langle x(t)\, y(t + \Delta t)\rangle. \tag{6}$$

$\langle\cdot\rangle$ denotes the time average. The relaxation time of $g(r = R)$ in response to changes in turbulent energy, $\tau_g \equiv \tau_{p\to g}$, is defined as the lag between P and $g(r = R)$, and can be decomposed into two contributions: $\tau_{p\to\varepsilon}$ and $\tau_{\varepsilon\to g}$, such that $\tau_g \approx \tau_{p\to\varepsilon} + \tau_{\varepsilon\to g}$. The case $(\text{St}_{\text{strong}}, \text{St}_{\text{weak}}) = (1.0, 0.5)$ was excluded due to the non-monotonic structure in the ε–g^* relationship, which prevented unambiguous identification of $\tau_{\varepsilon\to g}$. For both Stokes numbers, $\tau_{p\to\varepsilon} = 2.39$, indicating that the response of ε to the forcing is independent of the particle Stokes number, as expected. τ_g increases with Stokes number: $\tau_g \approx 3.44$ for $(0.4, 0.2)$ and $\tau_g \approx 4.42$ for $(4.0, 2.0)$. For both cases, $\tau_g \approx \tau_{p\to\varepsilon} + \tau_{\varepsilon\to g}$ holds. These results support the notion that the relaxation time is finite and of the order of the eddy turnover time.

Figure 2 shows g^* as a function of ε under fixed-interval forcing for three forcing periods ($T^* = 1.6$, 6.4, and 24.0). Here, $g^* \equiv g^{\text{NonEQ}}/\langle g^{\text{EQ}}\rangle$, where g^{NonEQ} is $g(r = R)$ and $\langle g^{\text{EQ}}\rangle$ is the time-averaged value obtained under steady forcing at the same time-averaged energy injection rate $\langle P\rangle$ as in the fixed-interval forcing case.. g^{EQ} represents the value predicted by the instantaneous equilibrium model, to which $g(r = R)$ converges under the instantaneous equilibrium as-

Table 1. The lags under random-interval forcing with $\lambda = 2.0$.

$(\mathrm{St}_{\mathrm{strong}}, \mathrm{St}_{\mathrm{weak}})$	$\tau_{p\to\varepsilon}$	$\tau_{\varepsilon\to g}$	$\tau_{p\to\varepsilon} + \tau_{\varepsilon\to g}$	$\tau_{p\to g}$
$(0.4, 0.2)$	2.39	0.82	3.21	3.44
$(4.0, 2.0)$	2.39	2.03	4.39	4.42

sumption at a given ε. Figures 2a, 2b, and 2c correspond to $(\mathrm{St}_{\mathrm{strong}}, \mathrm{St}_{\mathrm{weak}}) = (0.4, 0.2)$, $(1.0, 0.5)$, and $(4.0, 2.0)$, respectively. For long-period forcing ($T^* = 24.0 > \tau_g$), the trajectory forms a large hysteresis loop in the g^*–ε plane, indicating that g^* does not correspond one-to-one with ε. At $\varepsilon \approx 0.4$, g^* varies approximately between 0.6 and 1.2 depending on the flow history. For intermediate-period forcing ($T^* = 6.4 \sim \tau_g$), a smaller hysteresis loop is observed. For short-period forcing ($T^* = 1.6 < \tau_g$), ε and g^* remain nearly constant, and no hysteresis is observed. Hysteresis is observed for both long- and intermediate-period forcing across all Stokes numbers examined. This indicates that equilibrium-based models cannot accurately predict clustering in non-equilibrium turbulence when the forcing period is longer than or comparable to τ_g.

Conclusions

We performed direct numerical simulations of inertial particle motion in turbulent flows generated by unsteady forcing.

The turbulent flow generated by unsteady step forcing exhibited non-equilibrium scaling. This demonstrated that unsteady step forcing can generate non-equilibrium turbulence.

The relaxation time of $g(r = R)$ in response to changes in turbulent energy, τ_g, was estimated to be 3–4 T_e. These results support the notion that the relaxation time is finite and on the order of the eddy turnover time.

When the forcing period was longer than or comparable to τ_g, $g(r = R)$ exhibited history dependence. In some cases, $g(r = R)$ ranged from 0.6 to 1.2 times the value predicted by the instantaneous equilibrium model for the same ε. This indicates that equilibrium-based models cannot accurately predict clustering in non-equilibrium turbulence when the forcing period is longer than or comparable to τ_g.

These results suggest that constructing a clustering model that accounts for the relaxation time is essential for predicting clustering in non-equilibrium turbulence.

REFERENCES

Ayala, O., Rosa, B., Wang, L.-P. & Grabowski, W. W. 2008 Effects of turbulence on the geometric collision rate of sedimenting droplets. Part 2. theory and parameterization. *New J. Phys.* **10**, 075016.

Goto, S. & Vassilicos, J. C. 2015 Energy dissipation and flux laws for unsteady turbulence. *Phys. Lett. A* **379**, 1144–1148.

Harlow, F. H. & Welch, J. E. 1965 Numerical calculation of time-dependent viscous incompressible flow of fluid with free surface. *Phys. Fluids* **8**, 2182–2189.

Hirt, C. W. & Cook, J. L. 1972 Calculating three-dimensional flow around structures and over rough terrain. *J. Comput. Phys.* **10**, 324–340.

Ireland, P. J., Bragg, A. D. & Collins, L. R. 2016 The effect of Reynolds number on inertial particle dynamics in isotropic turbulence. Part 2. simulations with gravitational effects. *J. Fluid Mech.* **796**, 617–658.

Maxey, M. R. 1987 The gravitational settling of aerosol particles in homogeneous turbulence and random flow fields. *J. Fluid Mech.* **174**, 441–465.

Morinishi, Y., Lund, T. S., Vasilyev, O. V. & Moin, P. 1998 Fully conservative higher order finite difference schemes for incompressible flow. *J. Comput. Phys.* **143**, 90–124.

Onishi, R., Baba, Y. & Takahashi, K. 2011 Large-scale forcing with less communication in finite-difference simulations of stationary isotropic turbulence. *J. Comput. Phys.* **230**, 4088–4099.

Onishi, R. & Seifert, A. 2016 Reynolds-number dependence of turbulence enhancement on collision growth. *Atmos. Chem. Phys.* **16**, 12441–12455.

Rosa, B., Parishani, H., Ayala, O., Grabowski, W. W. & Wang, L.-P. 2013 Kinematic and dynamic collision statistics of cloud droplets from high-resolution simulations. *New Journal of Physics* **15**, 045032.

Rowe, P. N. & Henwood, G. A. 1961 Drag forces in a hydraulic model of a fluidized bed. Part I. *Trans. Inst. Chem. Eng.* **39**, 43–54.

Squires, K. D. & Eaton, J. K. 1991 Measurements of particle dispersion obtained from direct numerical simulations of isotropic turbulence. *J. Fluid Mech.* **226**, 1–35.

Tominaga, T. & Onishi, R. 2025 LCS.jl: A high-performance, multi-platform computational model in Julia for turbulent particle-laden flows.

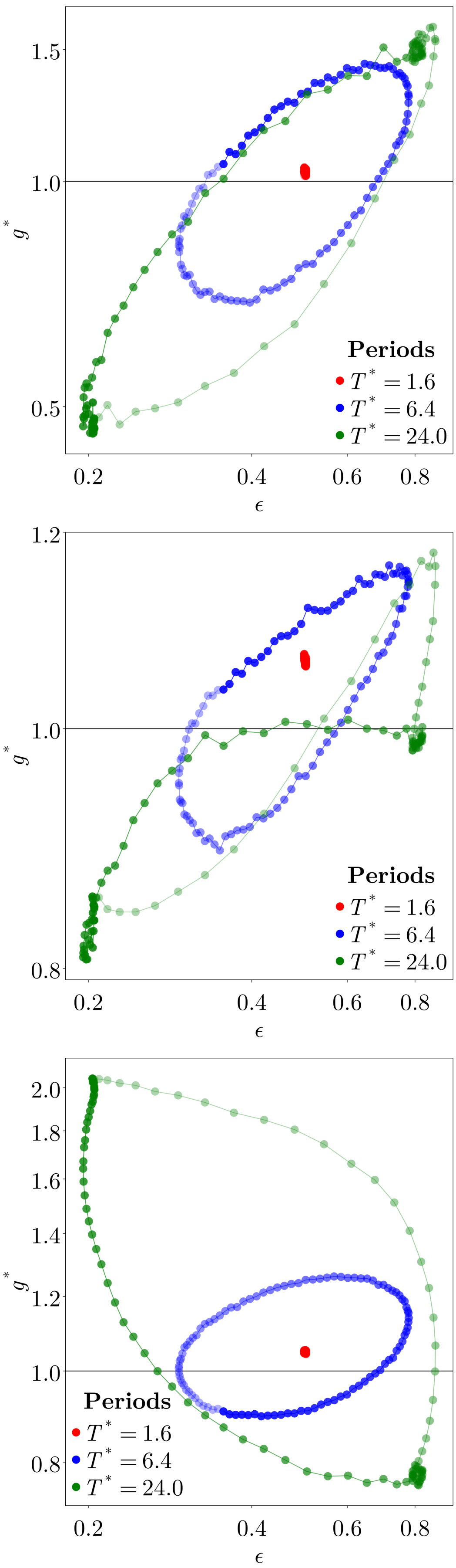

Figure 2. g^* as a function of ε under fixed-interval forcing for three forcing periods T^*. (a) $(\mathrm{St}_{\mathrm{strong}}, \mathrm{St}_{\mathrm{weak}}) = (0.4, 0.2)$, (b) $(1.0, 0.5)$, (c) $(4.0, 2.0)$. Color shading indicates temporal evolution, with darker colors representing later times.